Car-borne and UAV-borne mobile mapping of surface displacements with a compact repeat-pass interferometric SAR system at L-band

Othmar Frey
Gamma Remote Sensing /
Earth Observation & Remote Sensing,
ETH Zurich, Switzerland
Email: frey@gamma-rs.ch / otfrey@ethz.ch

Charles L. Werner
Gamma Remote Sensing
Switzerland
Email: cw@gamma-rs.ch

Roberto Coscione
Earth Observation & Remote Sensing,
ETH Zurich Switzerland

Abstract—In this paper, we present first results of car-borne and UAV-borne mobile mapping of potential surface displacements with a compact repeat-pass interferometric FMCW SAR system at L-band: (1) glacier-flow-induced displacements were measured at Stein glacier in the Swiss alps in car-borne mode along a slightly curved road section; (2) a valley slope was observed repeatedly using the vertical-take-off-and-landing (VTOL) UAV Scout B1-100 flown by Aeroscout. The SAR raw data were focused directly to an image grid in map coordinates, involving a digital elevation model and accurate GNSS/INS navigation data, by using a time-domain back-projection (TDBP) approach. These geocoded complex SAR images then allow to directly form differential interferograms in map coordinates. The feasibility of repeat-pass interferometry using our novel FMCW L-band SAR on mobile platforms such as a car or a UAV is successfully demonstrated with several data examples.

Index Terms—Synthetic aperture radar (SAR), SAR interferometry, mobile mapping, car-borne SAR, UAV, airborne SAR, terrestrial radar interferometer, repeat-pass interferometry, SAR imaging, focusing, back-projection, GPU, CUDA, interferometry, L-band, INS, GNSS.

I. INTRODUCTION

While current stationary terrestrial radar systems are bound to relatively high frequencies (many of them operating at Ku- or X-band) [1]–[3] to ensure a good cross-range resolution, an L-band SAR system, when operated in car-borne mode or UAV-borne mode, can still achieve a high cross-range resolution of about 0.5m up to a few meters. The cross-range resolution mostly depends on whether the full range-varying length of the synthetic aperture can be reached for the entire image, which again depends on geometric constraints imposed by the road (car-borne mode), possible flight tracks (airborne/UAV) and the topography.

An important advantage and a somewhat complementary property to the high-frequency stationary systems is the reduced temporal decorrelation at L-band. While the sensitivity to displacements is lower, the longer wavelength at L-band permits to acquire longer interferometric time series also in natural terrain, where the decorrelation time at Ku-band can be in the order of minutes or less.

In this paper, we demonstrate car-borne and UAV-borne mobile mapping of the line-of-sight component of (potential) surface displacements with our novel compact repeat-pass interferometric SAR system at L-band: (1) glacier-flow-induced displacements were measured at Stein glacier in the Swiss alps, in fall 2018, with our SAR system in car-borne mode along a slightly curved road section; (2) a valley slope was observed repeatedly in UAV-borne mode using the same SAR system mounted on-board Aeroscout's VTOL UAV Scout B1-100 in Wolfenschiessen (CH), in Feb./Mar. 2019.

TABLE I
GAMMA L-BAND SAR SPECIFICATIONS

Frequency within	1.2 - 1.4 GHz
used center freq.	1.325 GHz
wavelength at center freq.	22.6 cm
Chirp bandwidth	50 - 200 MHz
used bandwidth	100 MHz
range res. (@ 100 MHz BW)	1.5 m
Azim. res. (@ full SA)	≤ 0.5 m
Azim. res. (@ SA=250m, R=5km)	2.3 m
Type	FMCW
Chirp lengths	250 μs - 8 ms.
Transmit power	max. 10W (used: 5W)
Transmit channels	2 (alternating)
Receive channels	4 (simultaneous)
Elev. beamwidth (3dB)	40.0 deg
Azim. beamwidth (3dB)	40.0 deg
Elev. pointing angle	variable (config. dep.)
Radar hardware assembly	Pelicase 1450
Dimensions (l/w/h)	406/330/174 mm
Weight	7.65 kg

Fig. 1. (a) and (b) : Car-borne setup of the compact FMCW L-band SAR system with one transmit and three receive antennas as used in the Stein glacier demonstration campaign (only one receive channel used here), 2018. (c) Connector plate of the L-band radar with 2 alternating transmit channels and up to 4 simultaneous receive channels. (d) and (e): The L-band SAR mounted on Aeroscout's UAV Scout B1-100 at take-off (d) and during an interferometric repeat-pass SAR data acquisition (e) in Wolfenschiessen, central Switzerland, in winter 2019.
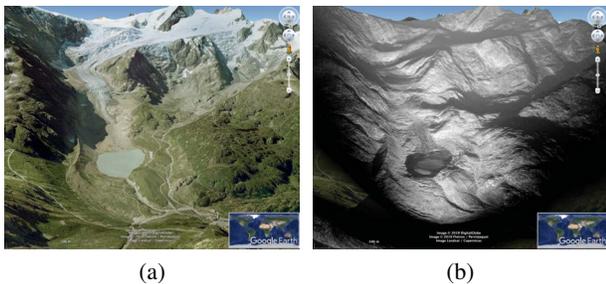

Fig. 2. a) Google Earth view of the Stein Glacier test site in Switzerland. b) Geocoded intensity image overlaid to Google Earth view as obtained from a car-borne L-band SAR acquisition with a 2ms chirp duration focused with TDBP to a DEM-based reconstruction grid in map coordinates.
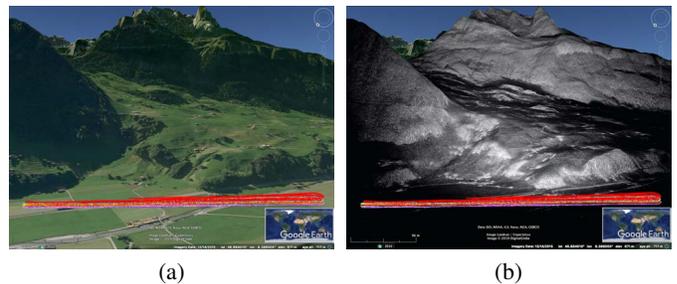

Fig. 3. a) Google Earth view of the UAV test site in Wolfenschiessen (CH). b) Geocoded intensity image overlaid to Google Earth view as obtained from a UAV-borne L-band SAR acquisition with a 2ms chirp duration focused with TDBP to a DEM-based reconstruction grid in map coordinates.

II. L-BAND RADAR HARDWARE, MEASUREMENT SETUPS, SAR IMAGING

In Table I a short summary of the specifications of the L-band FMCW SAR system is given. The L-band radar has 4 low-noise receiver channels that can operate simultaneously. A custom designed FPGA 14-bit/channel digitizer records from all four channels simultaneously and streams these data to an SSD. The radar instrument is controlled by a Linux-based computer. Transmitter max. output is 10W (5W used in our experiments) and includes a transmitter output switch that permits fully polarimetric data acquisition. The compact hardware implementation is aimed at UAV/air-borne and car-borne mobile mapping or rail-based terrestrial operation.

On the car, a high-precision iMAR iNAV-RQH ring-laser gyro INS/GNSS navigation system was used for navigation. In Fig. 1 (a) and (b), the measurement setup
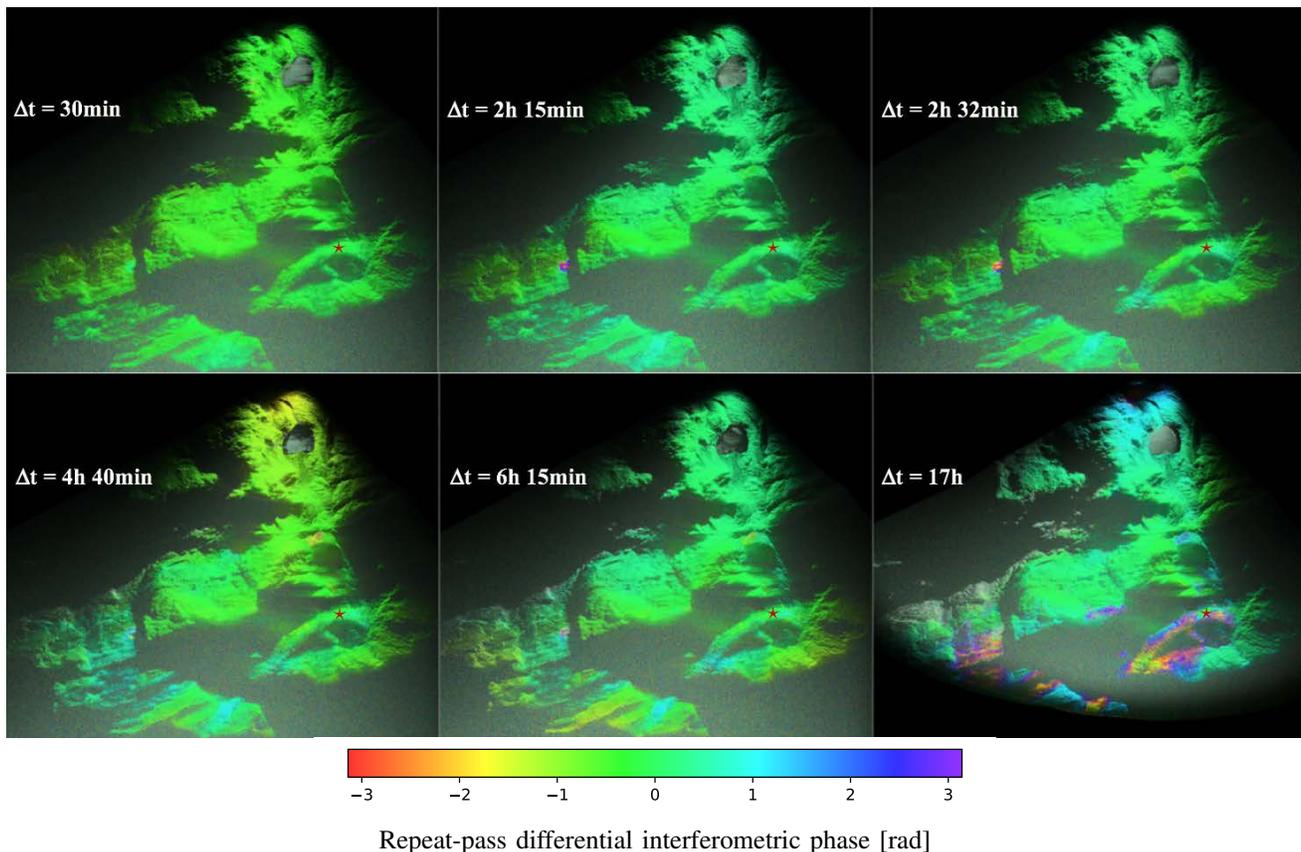
Fig. 4. Differential interferograms—with respect to a stable reference area on a rock surface (red star)—of the Stein Glacier and surrounding area in map coordinates with temporal baselines of 30min (upper left), 2h 15min (upper center), and 2h 32min (upper right), 4h 40min (lower left), 6h 15min (lower center), and 17h (lower right). The 17h interferogram is obtained between two acquisitions with 1ms chirp duration; hence the limited range distance of ca. 4.68 km. All the rest of them are acquired with a 2ms chirp. With a carrier frequency of 1.325 GHz (wave length of 22.6 cm) an interferometric phase value of 2π translates to a line-of-sight displacement of 11.3 cm.

for the car-borne case is shown: on the aluminium rack one transmit and 3 receive patch antennas are mounted in a side-looking configuration. In the lower row of Fig. 1 the L-band SAR (one transmit and one receive antenna) mounted on Aeroscout's UAV Scout B1-100 is shown at take-off (d) and during an interferometric repeat-pass SAR data acquisition (e) in central Switzerland. The UAV is equipped with a Honeywell HGUIDE n580 INS/GNSS system. For both cases, GNSS data is processed in post-processing kinematic mode relative to an ad-hoc local GNSS reference station in the field followed by a loosely-coupled GNSS/INS integration.

The car-borne or UAV-borne SAR data is focused along a synthetic aperture (of approx. 200-250m) using a CUDA/ANSI C [4] implementation of a time-domain back-projection (TDBP) approach [5], [6] adapted to FMCW systems [4], [7]–[9] leading to focused complex SAR images directly in map coordinates. This approach allows then to directly calculate the differential

interferograms in map coordinates. Since highly-precise INS/GNSS systems were used for positioning and attitude determination of the SAR system the azimuth-varying baselines (due to the slightly different repeated tracks) are well-known and the topography induced phase can be removed largely by means of the TDBP-based focusing procedure.

III. RESULTS

Figs. 2 & 3 show a scene overview for the two test sites and geocoded L-band SAR intensity images obtained in car-borne and UAV-borne mode are also depicted. In Fig. 4, differential interferograms of the Stein Glacier and the surrounding area are shown for different temporal baselines ranging from 30 min to 17h. The 17h interferogram is obtained between two acquisitions with 1ms chirp duration; therefore the range distance is limited to 4.68km in this case. All other interferograms shown are based on acquisitions with a chirp
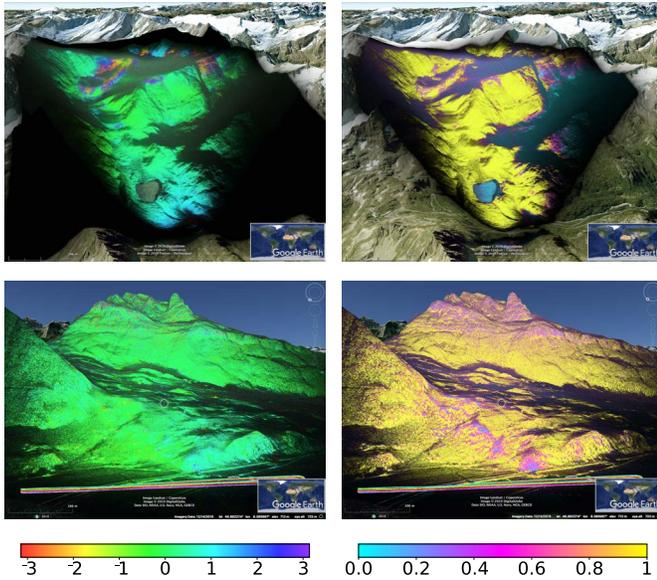
Fig. 5. Upper row: car-borne SAR differential interferogram (left) and coherence (right)—each blended with a multi-look intensity image—with a temporal baseline of 1020 min (17h) of the Stein Glacier and surrounding area in a 3-D view. Lower row: UAV-borne differential interferometric phase (left) and coherence (right) for nominally zero spatial baseline and a temporal baseline of 3 minutes. With the exception of forested areas in the near range and areas with severe foreshortening a very high coherence is obtained and the interferometric phase is also stable.

duration of 2ms. With a carrier frequency of 1.325 GHz (wavelength of 22.6cm) an interferometric phase value of 2π translates to a line-of-sight displacement of 11.3cm. In Fig. 5, 3-D visualisations of the interferometric phase and coherence are shown for a temporal baseline of 17h for the glacier data set and for a temporal baseline of 3min for the UAV-borne data set. The flight tube of the two UAV-borne repeat-tracks are within 1m radius.

IV. DISCUSSION

The stable phase of the short-term (30min in the car-borne case, 3min in the UAV-borne case) repeat-pass interferograms confirms that the SAR image focusing is of high quality, that the positioning solution is of sufficient quality to obtain only very small residual unknown positioning errors compared to the wavelength at L-band, and that troposphere-induced variations are also small for these short intervals. This indicates a good quality of the entire repeat-pass InSAR system incl. the processing chain for both, car-borne and UAV-borne cases. Looking at the time series obtained for the Stein glacier, a small area of the glacier with a substantial motion is already well observed in the second interferogram pair while most areas of the glacier are moving much slower.

Gradually the displacement phase due to glacier flow increases over time, with the 17h temporal interferogram reaching an entire phase cycle corresponding to line-of-sight displacements of around 11cm and more. With increasing temporal baselines more low-frequency phase trends gradually appear indicating temporal changes of the tropospheric conditions. For the UAV-borne case, except in forested areas in the near range and areas with strong foreshortening, a high coherence is obtained and the InSAR phase is also stable—with slightly increased phases and a reduced coherence in the forest due to a mismatch of the vegetation height versus the DEM used and volume decorrelation, resp.—demonstrating the good performance of the repeat-pass InSAR system.

REFERENCES

[1] C. L. Werner, T. Strozzi, A. Wiesmann, and U. Wegmuller, "A real-aperture radar for ground-based differential interferometry," in *Proc. IEEE Int. Geosci. Remote Sens. Symp.*, vol. 3, July 2008, pp. 210–213.

[2] G. Luzi, M. Pieraccini, D. Mecatti, L. Noferini, G. Guidi, F. Moia, and C. Atzeni, "Ground-based radar interferometry for landslides monitoring: atmospheric and instrumental decorrelation sources on experimental data," *IEEE Trans. Geosci. Remote Sens.*, vol. 42, no. 11, pp. 2454–2466, Nov. 2004.

[3] D. Leva, G. Nico, D. Tarchi, J. Fortuny-Guasch, and A. Sieber, "Temporal analysis of a landslide by means of a ground-based SAR interferometer," *IEEE Trans. Geosci. Remote Sens.*, vol. 41, no. 4, pp. 745–752, Apr. 2003.

[4] O. Frey, C. L. Werner, and U. Wegmuller, "GPU-based parallelized time-domain back-projection processing for agile SAR platforms," in *Proc. IEEE Int. Geosci. Remote Sens. Symp.*, July 2014, pp. 1132–1135.

[5] O. Frey, C. Magnard, M. Rüegg, and E. Meier, "Focusing of airborne synthetic aperture radar data from highly nonlinear flight tracks," *IEEE Trans. Geosci. Remote Sens.*, vol. 47, no. 6, pp. 1844–1858, June 2009.

[6] O. Frey, E. Meier, and D. Nüesch, "Processing SAR data of rugged terrain by time-domain back-projection," in *SPIE Vol. 5980: SAR Image Analysis, Modeling, and Techniques X*, 2005.

[7] A. Ribalta, "Time-domain reconstruction algorithms for FMCW-SAR," *IEEE Geosci. Remote Sens. Lett.*, vol. 8, no. 3, pp. 396–400, May 2011.

[8] O. Frey, C. L. Werner, U. Wegmuller, A. Wiesmann, D. Henke, and C. Magnard, "A car-borne SAR and InSAR experiment," in *Proc. IEEE Int. Geosci. Remote Sens. Symp.*, 2013, pp. 93–96.

[9] C. Stringham and D. G. Long, "GPU processing for UAS-based LFM-CW stripmap SAR," *Photogrammetric Engineering & Remote Sensing*, vol. 80, no. 12, pp. 1107–1115, 2014.